Electrochimica Acta 304 (2019) 437–446

Contents lists available at ScienceDirect

Electrochimica Acta

journal homepage: www.elsevier.com/locate/electacta

Furfuryl alcohol derived high-end carbons for ultrafast dual carbon lithium ion capacitors

María Arnaiz [a], Vinod Nair [b], Shantanu Mitra [b], Jon Ajuria [a, *]

[a] CIC Energigune, Albert Einstein 48, Technology Park of Alava, 01510, Miñano, Alava, Spain
[b] Farad Power, Inc, 428 Oakmead Parkway, Sunnyvale, CA94085, USA

ARTICLE INFO

Article history:
Received 13 December 2018
Received in revised form
21 February 2019
Accepted 4 March 2019
Available online 5 March 2019

Keywords:
Furfuryl alcohol
Activated carbon
Hard carbon
Lithium ion capacitor
EDLC
Supercapacitor

ABSTRACT

In this work, a lithium ion capacitor (LIC) based on carbon electrodes prepared from furfuryl alcohol-derived polymers is presented. While furfuryl alcohol is not a new carbon precursor, it has been evaluated in the past mainly for negative electrodes with Li-ion insertion. Here we describe both an activated carbon (AC) and a hard carbon (HC) made from the same furfuryl alcohol-derived polymers, for both electrodes of the LIC. The polymerization technique used to make carbon from the furfuryl alcohol precursor is different from all the methods described earlier, and is flexible enough to make soft, high surface area AC, as well as a denser, low surface area HC. The HC and the HC-based negative electrode used in this study are targeted at a high-energy and high-power LIC application by specifically reducing the carbon particle size to sub-micrometric levels, using a HC with a specific surface area of ~300 $m^2 g^{-1}$ and keeping the electrode mass loading to <2 mg cm^{-2}. The HC delivers a stable capacity of ~400 mAh g^{-1} *vs.* Li^+/Li at C/10, with excellent capacity retention of 50% at 10C (>200 mAh g^{-1}) and 25% at 50C (~100 mAh g^{-1}). The AC used for the capacitor-type positive electrode was activated to a specific surface area of ~1670 $m^2 g^{-1}$. For comparison purposes, a symmetric electric double layer capacitor (EDLC) using the same AC, in a 1.5 M Et_4NBF_4 (acetonitrile) electrolyte, was also fabricated. Overall, the LIC showed considerably higher energy density over its EDLC counterpart, delivering a maximum energy density (based on the total electrode active mass weight) of 150 Wh kg^{-1}_{AM} at a power density of 150 W kg^{-1}_{AM}, with a 66% retention of the initial energy at the highly demanding 10,000 W kg^{-1}_{AM} power peak point. Additionally, long cycle life was measured, with 83% capacitance retention after 10,000 cycles.

1. Introduction

Hybrid supercapacitor configurations like the so-called lithium ion capacitors (LICs) have been of interest lately, in light of their ability to overcome the energy density limitations of symmetric supercapacitors. The energy storage mechanism operating in a symmetric supercapacitor is based entirely on capacitive charge storage, which is non-faradaic in nature. Hybrid supercapacitors, on the other hand, comprising a negative battery-type electrode (with faradaic charge storage mechanism based on Li-ion intercalation into the electrode material) and a positive capacitor-type electrode, have been recently commercialized [1–4]. The most widely studied configuration of LICs is based on dual carbon electrodes, with graphite being the preferred option to replace the capacitive activated carbon (AC) at the negative electrode of the symmetric supercapacitor. Meanwhile, AC remains the popular choice for the positive electrode [5–8]. However, the increasing need to withstand high-power peaks in various applications (*e.g.* transportation, consumer, aerospace etc.), has focused attention on replacing graphite -with its limited Li-ion intercalation capacity and rate capability- with materials capable of higher capacity and charge/discharge rate-capability.

Several graphite-replacement materials have shown promise, including some advanced carbons [9–11], $Li_4Ti_5O_{12}$ [12–14], Li_3VO_4 [15,16] and some metal alloys [17–19]. Of the carbonaceous alternatives to graphite, both soft carbons (SCs) and hard carbons (HCs) have been investigated [20–24]. Turns out, the disordered nature of HCs with its limited microscopic crystalline graphite-like regions, allows insertion of Li-ion on both sides of the graphene sheets within the microscopic graphite-like regions (potentially doubling the theoretical capacity compared to graphite), consequently allowing for a potentially higher charge rate in the device. This has

* Corresponding author.
E-mail address: jajuria@cicenergigune.com (J. Ajuria).

https://doi.org/10.1016/j.electacta.2019.03.029
0013-4686/

made HC an attractive option for the negative electrode of high-power, high-energy LICs.

Dual carbon-based LICs need to also address the fact that they lack an internal source of lithium to compensate for the first cycle irreversibility. In this regard, graphite has the advantage over HC due to its lower first cycle irreversibility (~5–10% compared to HC's ~ 20–30%), whereby it consumes less Li in the solid electrolyte interphase (SEI) formation. Pre-lithiation is then an attractive option to compensate for this. Recently, the use of sacrificial salts for pre-lithiation of graphite-based LICs was demonstrated [25]. For HC-based LICs, stabilized lithium metal powder (SLMP) and metallic lithium strip forms were shown to be effective pre-lithiation strategies [26,27]. Very recently, JSR Micro announced an 'out-of-cell' roll-to-roll pre-lithiation approach that will enable the use of materials like HCs with high first cycle irreversibility in LIC configurations [28].

For the AC used in the positive electrode of the LICs, there is little controversy regarding its suitability for the application. Since the charge storage mechanism here is capacitive, it is not the limiting factor in the performance of the LIC, although the AC still needs to be of high specific surface area, with high purity (impurities like Fe, Cu, Cr need to be at <20 ppm levels). A large number of natural sources have been evaluated as precursors for AC. These include biomass waste [29], such as fruit peals [30,31], pits [32,33], seeds [34,35], potato starch [36], algae [37], or nutshells [9]. Most of these natural precursors suffer from batch to batch variation due to their relatively high impurity content which is also often dependent on its region of origin. The most popular natural precursor today is coconut shell, and ACs based on this precursor have been widely commercialized (*e.g.* YP-50 and YP-80 branded AC offered by Kuraray Chemical, Tokyo, Japan) due to their optimum combination of cost and performance. However, their performance is still capped, prompting the evaluation of synthetic precursors with inherently lower impurity content. Synthetic polymers materials like phenolic resins [38,39] and polyacrilates [40] have been studied. However, the cost and/or toxicity of these polymer precursors is seen as a disadvantage, and has resulted in the evaluation of alternative polymers, like those based on furfuryl alcohol (FA).

Most of the FA-based carbons till now have been HCs [41,42]. The fabrication methods used for these were complex, involving reflux heating, vacuum distillation and high temperature heating in pressure vessels. Recently, a much simpler process to synthesize HC from FA -involving room temperature polymerization, without the use of strong inorganic acids- was described [43]. HCs with X-ray diffraction peaks corresponding to microscopic graphene sheet spacing (*i.e.* the 'c'/2 lattice parameter, also referred to as the 'd_{002}' spacing) of up to 3.9 Å were synthesized from FA using weak organic acids. The corresponding d_{002} value for graphite is 3.35 Å, although the intensity of the X-ray diffraction peak is much larger and sharper for graphite, indicating its fully ordered structure. Thus, HCs with their higher d_{002} spacing have theoretically higher Li-ion intercalation capabilities than graphite, resulting in higher capacity values. One such HC, synthesized from FA, has been used for the negative electrode of the developed LIC.

A new process to synthesize ACs from the same FA precursor materials has also been described [44]. This process is similar to that for the HC in its simplicity (*i.e.* no complex vacuum distillation or pressurized heating), but differs from the previously mentioned process in that it has different additives and uses different heating rates and temperatures. Following polymerization, the material is carbonized and activated to result in a high surface area AC, with low impurity levels. An AC synthesized from FA using this method has been used for the positive electrode of the LIC investigated in this study. This is unique since synthesizing a HC and an AC from the same synthetic precursor has not been reported on till date. Further fine tuning of the electrode fabrication protocols allowed to develop both Li insertion faradaic and ion adsorption capacitive carbon based electrodes with high capacity and excellent rate capability features. In combination, a long lasting ultrafast LIC was also developed, delivering high energy at high power.

2. Experimental

2.1. Material synthesis

The HC used in this study was prepared from FA (#W249106, from Sigma Aldrich, St. Louis, MO, USA) by a process of polymerization and carbonization. FA was mixed with a combination of organic acids: oxalic acid (#75688, from Sigma Aldrich St. Louis, MO., USA), maleic acid (#M0375, from Sigma Aldrich St. Louis, MO., USA), and L-(+)-tartaric acid (#T109, from Sigma Aldrich St. Louis, MO., USA), in a 10:1 ratio (by weight) of FA to total organic acids. The mixture was then polymerized by holding it at room temperature for a period of 48 h, prior to heating at 50 °C, 120 °C and 200 °C for 24 h, respectively, under air. A dense polymer was obtained at this stage, which was then carbonized by heating under N_2 (flowing @ 2 L min^{-1}) at temperatures of 800 °C (for 1 h), followed by a calcination step of 1 h at 1000 °C under N_2 (flowing @ 2 L min^{-1}). The HC was then manually coarse-ground in a hard porcelain mortar/pestle, before being ball-milled using a jar and balls made of zirconia with a 1:30 HC:ball mass ratio in a Pulverisette 5 (Fritsch International, Germany). Milling was performed for 90 min.

The AC was also prepared from FA by a process of polymerization, carbonization, and activation. Specifically, FA (#W249106, from Sigma Aldrich, St. Louis, MO, USA) was mixed with a combination of organic acids: oxalic acid (#75688, from Sigma Aldrich St. Louis, MO., USA), maleic acid (#M0375, from Sigma Aldrich St. Louis, MO., USA), and L-(+)-tartaric acid (#T109, from Sigma Aldrich St. Louis, MO., USA) in a 10:1 ratio (by weight) of FA to total organic acids. To this mixture, carbon black powder (C-NERGY C-45, from Imerys, Willebroek, Belgium) was added (2 wt % relative to the FA) and stirred in. The mixture was then polymerized by first holding at room temperatures for 24 h, followed by heating at 120 °C and 200 °C for 24 h respectively, under air. A solid polymer was obtained, with a lower density than that obtained for the HC material. This solid polymer was then carbonized at 600 °C under N_2 (flowing @ 2 L min^{-1}) for 1 h. Activation was performed by heating the carbonized material under CO_2 (flowing @ 4 L min^{-1}) at 1000 °C for 3 h. This resulted in an AC with a specific surface area (SSA) in the range of 1600–1700 m^2 g^{-1}. The AC was then manually coarse-ground in a hard porcelain mortar/pestle, before being ball-milled using a jar and balls made of zirconia with a 1:30 AC:ball mass ratio in a Pulverisette 5 (Fritsch International, Germany). Milling was performed for 15 min. The process for both carbons is schematically depicted in Fig. 1.

2.2. Material characterization

The AC and HC materials synthesized by the methods described above were then characterized for surface area, porosity, structure, morphology and surface composition. For surface area and porosity, N_2 adsorption isotherms were measured at −195.8 °C using Micromeritics ASAP 2020 instrument for relative pressure values (P/P_0) between 10^{-8} and 0.995 for samples preliminarily outgassed for 8 h at 300 °C. The SSA values and pore size distribution (PSD) were calculated by applying the 2D Non-Local Density Functional Theory (2D-NLDFT) treatment to N_2 adsorption branch isotherm using the data reduction software SAIEUS. For structure analysis, X-ray diffraction (XRD) patterns were recorded on powdered samples

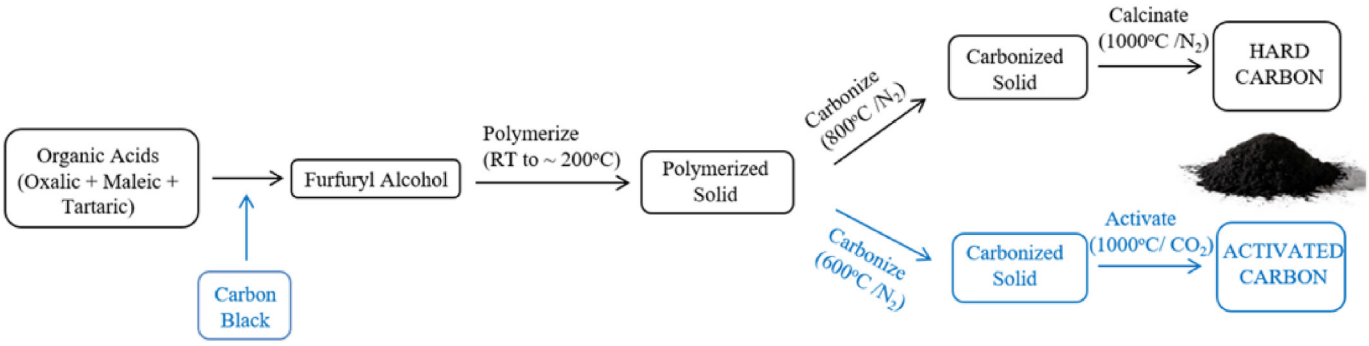

Fig. 1. Synthesis method for furfuryl-alcohol-based hard carbon and activated carbon, used in this study.

in a Bruker D8 X-ray diffractometer. Data were collected at 40 kV and 30 mA using Cu K_α radiation over a 2θ range from 15° to 80°. Additionally, Raman spectroscopy was also used. Raman spectra were recorded with a Renishaw spectrometer (Nanonics Multiview 2000) operating at an excitation wavelength of 532 nm. The spectra were acquired after 10 s of exposition time of the laser beam to the sample. The morphology was studied using scanning electron microscopy (SEM). SEM images were acquired with a field emission Quanta 200 FEG microscope from FEI. Surface composition was measured using X-ray photoelectron spectroscopy (XPS). Measurements were carried out in a UHV spectrometer chamber with base pressure below 10^{-10} mbar. The chamber features a hemispherical analyzer PHOIBOS 150 with a 2D-DLD detector (SPECS) and monochromatic X-ray source FOCUS 500 (SPECS) with two anodes: Al Ka (hn ¼ 1486.74 eV) and Ag La (hn ¼ 2984.3 eV).

2.3. Electrode preparation, cell assembly and electrochemical characterization

The electrode slurry for the negative electrode was prepared by mixing the HC, Super C C65 carbon black (Imerys Graphite & Carbon, Willebroek, Belgium) and polyvinylidene fluoride (PVdF), as the binder, in a mass ratio of 90:5:5 in *N*-methyl-2-pyrrolidone (NMP); followed by vigorous stirring for 1 h using a magnetic stirrer. For the positive electrode, the slurry was prepared by mixing the AC, Super C C65 (Imerys Graphite & Carbon, Willebroek, Belgium) and PVdF, as the binder, in a mass ratio of 90:5:5 in NMP; also followed by vigorous stirring for 1 h using a magnetic stirrer. The HC slurry was deposited onto a copper current collector sheet, whereas the AC slurry was laminated onto an aluminum current collector sheet. Laminates were immediately transferred into a vacuum oven and dried at 80 °C under constant vacuum for 12 h, before 0.95 cm^2 circular individual electrodes were cut out. HC electrodes weighed between 1 and 1.5 mg cm^{-2} with a thickness value between 30 and 50 μm, while AC electrodes were within 2–3 mg cm^{-2} with a thickness of 60–80 μm, resulting in a mass ratio of 1:2 for the HC:AC electrodes. All electrodes were dried overnight at 120 °C, in a vacuum oven before being tested. The HC-based electrodes were characterized in a three-electrode Swagelok® airtight system using metallic Li, both as the counter and the reference electrode. AC electrodes were also preliminarily tested in a three-electrode Swagelok® airtight system using the AC as the working electrode, commercial activated carbon YP-80F as the counter electrode and metallic Li as the reference electrode. The mass of the counter electrode was a few times higher than that of the working electrode to ensure that its higher surface area and the narrow potential range prevent electrolyte degradation. Finally, hybrid supercapacitor LIC cells were assembled in a three electrode Swagelok® system with a metallic Li reference, using stainless steel current collectors and a porous glass fiber (Whatman GFB) membrane separator. 1 M $LiPF_6$ in 1:1 (EC:DMC) (Solvionic) was used as the electrolyte. The EDLC assembled for comparison, was built in a two electrode Swagelok® system using symmetric FA-derived AC electrodes from the same AC material used in the LIC. Stainless steel current collectors and a porous glass fiber (Whatman GFB) membrane separator immersed in 1.5 M Et_4NBF_4(acetonitrile, ACN) were used. Cyclic voltammetry (CV), Galvanostatic (GA) charge-discharge cycling and electrochemical impedance spectroscopy (EIS) measurements were conducted using a multichannel VMP3 generator (Biologic, France) applying a low sinusoidal amplitude alternating voltage of 10 mV over zero current potential (OCP) at frequencies from 1 MHz to 10 mHz.

3. Results and discussion

Fig. 2 shows micrographs of typical HC and AC particles, before and after ball milling. Particles going into ball milling, for both the HC and AC, are on the order of several hundred microns (HC: Fig. 2a; AC: Fig. 2b). The HC particles before milling are characterized by flat surfaces, while the AC particles show a sponge-like surface. As mentioned earlier, ball milling on the HC was performed to give a sub-micron particle size. This is important in order to obtain the desired performance for high power applications, since the storage mechanism of the HC is dominated by slower redox reactions (compared to capacitive storage for the AC). Fig. 2c shows a ball milled HC agglomerate, with a higher magnification inset showing the smaller sub-micron individual particles. Fig. 2d shows the milled AC particles, which were milled down to a larger size compared to the HC, in the range of 10–20 μm.

The structural characterization of the synthetized carbons is shown in Fig. 3. The XRD pattern of the carbons is shown in Fig. 3a. The broad diffraction peaks at ~24° and ~43°, corresponding to (002) and (100) reflections, are characteristic of generally disordered carbons with a low degree of graphitization. The interlayer spacing of the crystalline structure d_{002} was found to be 3.7 Å. The thickness of the graphitic domains (L_c) was calculated using the Scherrer equation and the size was found to be 11.7 Å, indicating that they are formed by stacking of 2 or 3 layers of graphene. The structure of the carbons was further investigated by Raman spectroscopy. As shown in Fig. 3b, both carbons exhibit a G-band at ~1580 cm^{-1} (in-plane C-C vibrations) and a D-band at ~1340 cm^{-1} (a breathing mode only active when there is disorder in the structure). The ratio between peak integrated areas of the I_D and I_G bands turned out to be 0.66 and 0.63 respectively, values considerably below 1, confirming the disordered morphology and the low graphitization degree of both carbons [32]. Additionally, two broad peaks can be identified in the region 2500-3000 cm^{-1} corresponding to 2D and D + G bands.

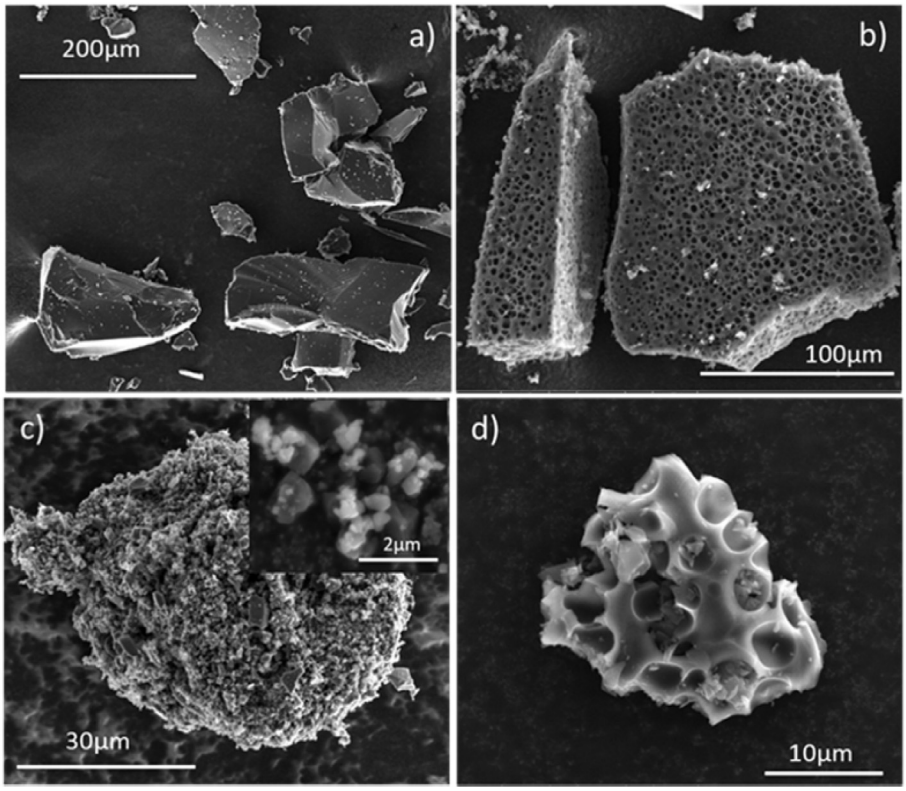

Fig. 2. SEM micrographs of a) as synthetized HC, b) as synthetized AC, c) ball milled HC, inset: magnification of the agglomerate surface and d) ball milled AC particle.

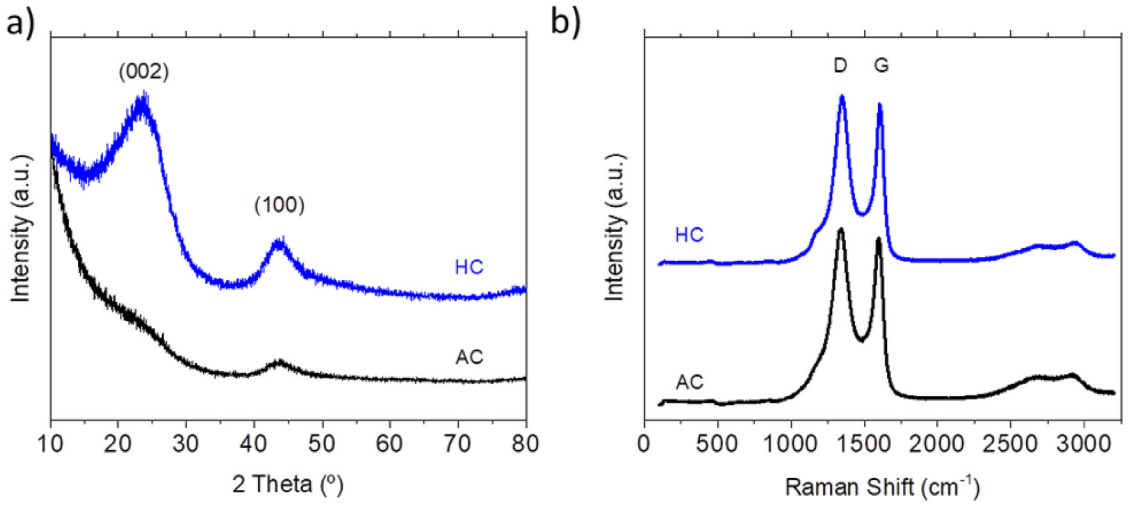

Fig. 3. Structural characterization of the synthetized carbons: a) XRD patterns and b) Raman spectra.

Textural properties of the carbons were characterized by using gas adsorption-desorption isotherms. The porosity of the AC was studied by analyzing the N_2 adsorption branch from which PSD was calculated using the 2D-NLDFT theory (see Fig. 4a and b). As expected, a type I isotherm (IUPAC classification) is obtained. This is typical of microporous carbons where pore filling occurs at low pressure and then saturates. The DFT-SSA value is 1672 $m^2 g^{-1}$ and PSD reveals a broad pore distribution limited to the micropore region with a mean pore size of 1.32 nm (Fig. 4b). Meanwhile, the surface texture of HCs is generally known to be defined by ultramicropores that need to be measured using CO_2 adsorptive gas (pore sizes are typically below ~ 6 Å). Thus, the porosity of the HC was measured by analyzing the adsorption branch obtained from the CO_2 isotherm, which also turned out to be type I. In Fig. 4d, PSD estimated for the HC using the 2D-NLDFT theory confirms the ultramicroporous nature of the HC, with a calculated SSA of 290 $m^2 g^{-1}$ and a mean pore size of 0.6 nm. The attainment of such a high SSA is not trivial, but a consequence of the specifically design synthetic route in view of the impact that a high SSA might have in power performance. A similar high SSA, with good cycle life was found earlier in a HC derived from peanut shells [9].

Fig. 5 shows the electrochemical characterization of the HC. In

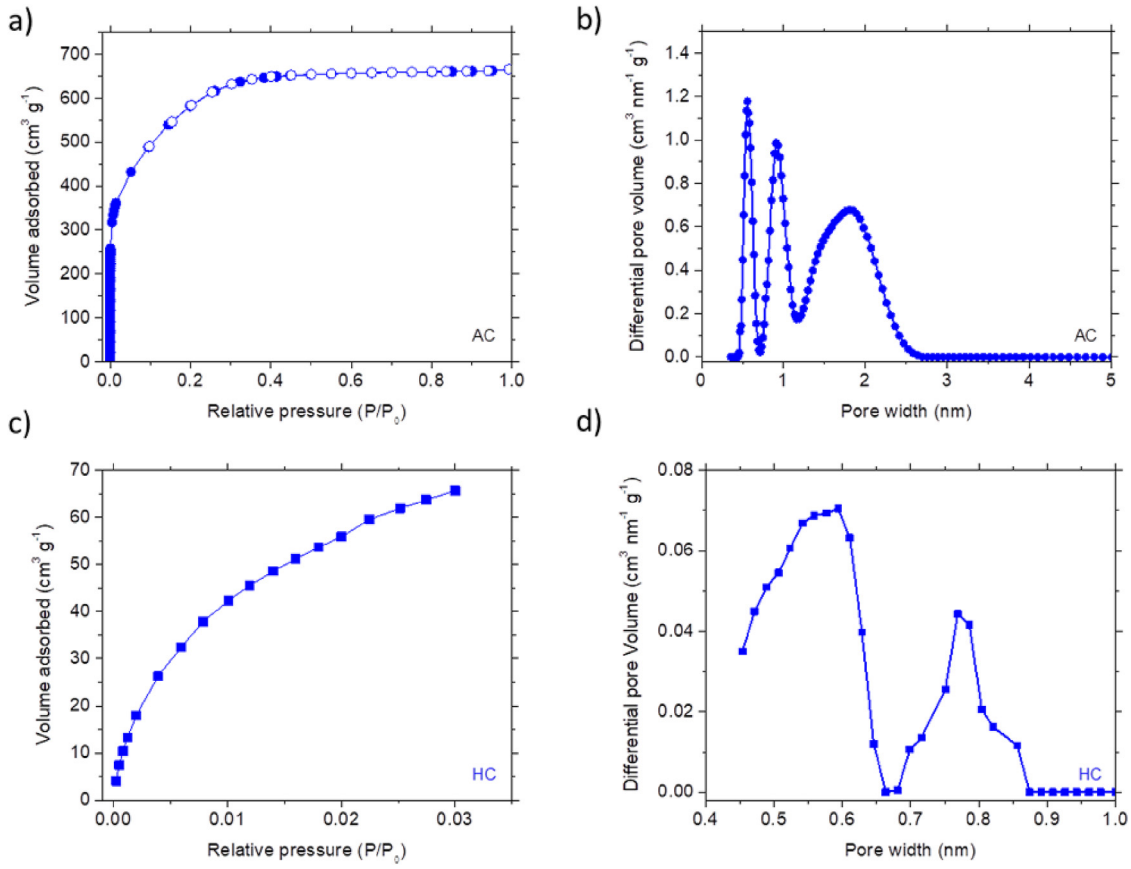

Fig. 4. Textural characterization of the synthetized carbons: a) N_2 adsorption-desorption isotherm of the AC, b) Pore size distribution of the AC calculated from the N_2 adsorption isotherm by applying the 2D-NLDFT model, c) CO_2 adsorption isotherm of the HC and d) Pore size distribution of the HC calculated from the CO_2 adsorption isotherm by applying the 2D-NLDFT model.

Fig. 5a, the EIS measurement carried out at OCP before cycling shows a small semicircle, which indicates a rather low charge transfer resistance and good transport through the electrode. Furthermore, at the lowest functional potential of the electrode (*i.e.* at 0.1 V *vs.* Li^+/Li), where maximum Li^+ insertion within the electrode is achieved, thus, where charge transfer and transport conditions are most hindered, the semicircle is even lower, indicating very little resistance compared to commonly reported values [45]. It thus appears that the low mass loading (~1.5 mg cm^{-2}) and small particle size (~1 μm) facilitate ion diffusion and electron transport, thereby playing a key role in minimizing electrode resistance. Fig. 5b shows the 1st and the 10th voltammograms taken at 1 mV s^{-1}. The first cycle shows a broad peak centered between ~1.0–0.6 V corresponding to the SEI formation due to carbonate solvent decomposition. The reductive decomposition of organic compounds in the electrolyte continues down to ~0.25 V, where ion insertion into nanopores starts. Generally, the SEI is expected to keep growing, however, in our case there is already no significant evidence of SEI formation by the 10th cycle, and the voltammogram shows a reversible broad oxidation/reduction peak below 1 V. The GA charge-discharge profiles of the HC are shown in Fig. 5c, with smooth slopes for all the delivered capacity range, and without the typical plateau component below 0.2 V. The first charge run at C/10 (considering C to be 372 mAh g^{-1}) delivers a total specific capacity of 1194 mAh g^{-1} while the subsequent discharge only reaches 423 mAh g^{-1}, accounting for a first cycle coulombic efficiency (CE) of 41%. The high irreversible capacity observed in the first cycle is ascribed to the low particle size of the HC that increases the electrode area and subsequently also the SEI formation. Subsequent charge-discharge profiles show similar slopes (without the plateau regions), even with very large applied current densities. This lack of the plateau region allows for good capacity values at these large current densities, since a plateau region in the GA slopes represents capacity that cannot be accessed at high applied current density. The rate capability test carried out on the HC electrode (Fig. 5d) presents excellent capacity retention; over 200 mAh g^{-1} delivered at 10C representing 50% of the initial reversible capacity set in the 5th cycle and *ca.* 100 mAh g^{-1} at 50C representing 25% of the initial capacity. At 100C, *i.e.* at a discharge time of 6 s, the HC is delivering 50 mAh g^{-1}, ensuring not only the high energy inherent to the HCs but also the high power required for supercapacitors. Nevertheless, test back to C/10 reveals a decrease in the CE to about 97–98%. This CE reduction may be the result of the mechanical stress induced when such high current densities are used on the device, resulting in some detrimental heat generation. Thus, a stability test for the HC within its full operative potential window (0.002–2 V *vs.* Li^+/Li) at 50C was run, limiting the discharge time to *ca.* 60 s. This resulted in an excellent capacity retention of 73% after 1,000 cycles (see Fig S1). Taking into account that a much narrower potential window will be used on the full device, the lifespan is expected to greatly increase when operating in a full system. Thus, by controlling the mass loading of the electrode and the particle size of the HC, a battery-type electrode based on faradaic reactions and characterized by high power capability with good cycle life, has been demonstrated from a FA-derived HC.

In Fig. 6 the electrochemical characterization of the AC is shown

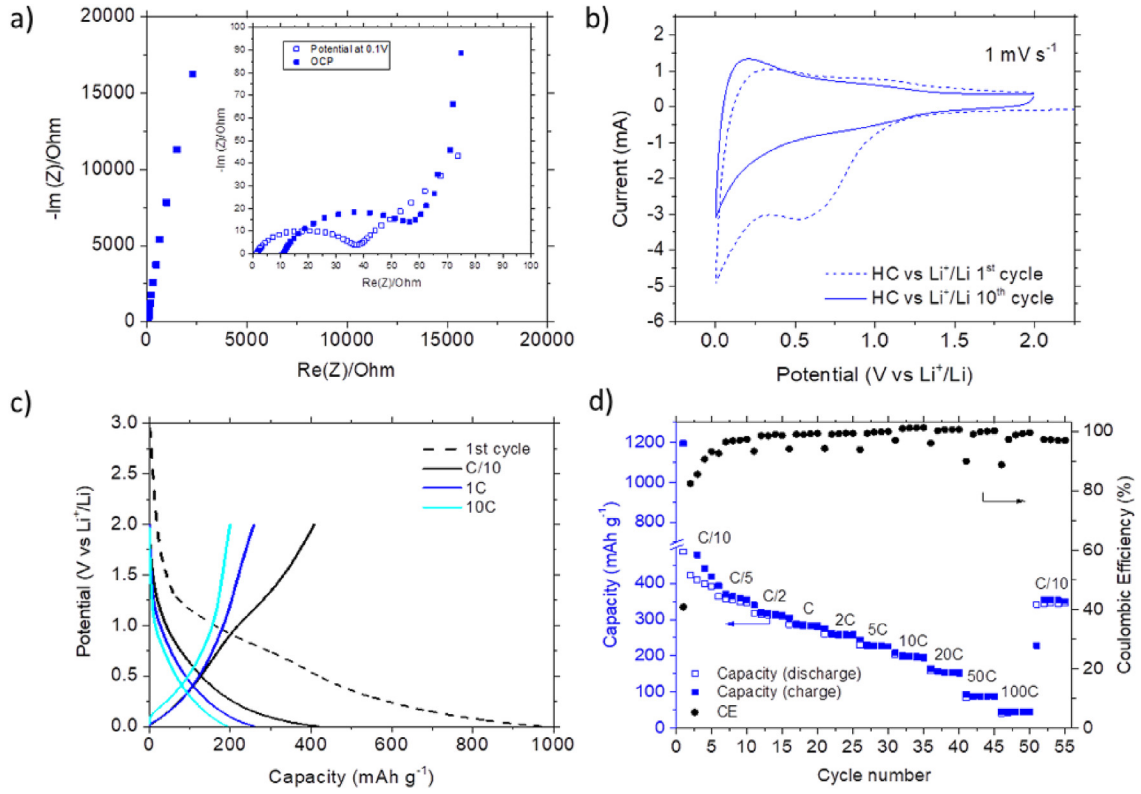

Fig. 5. a) EIS at OCP potential. b), c) and d) Electrochemical characterization of the HC tested between 0.002 and 2 V *vs.* Li^+/Li: CV, GA charge-discharge profiles and rate capability test, respectively.

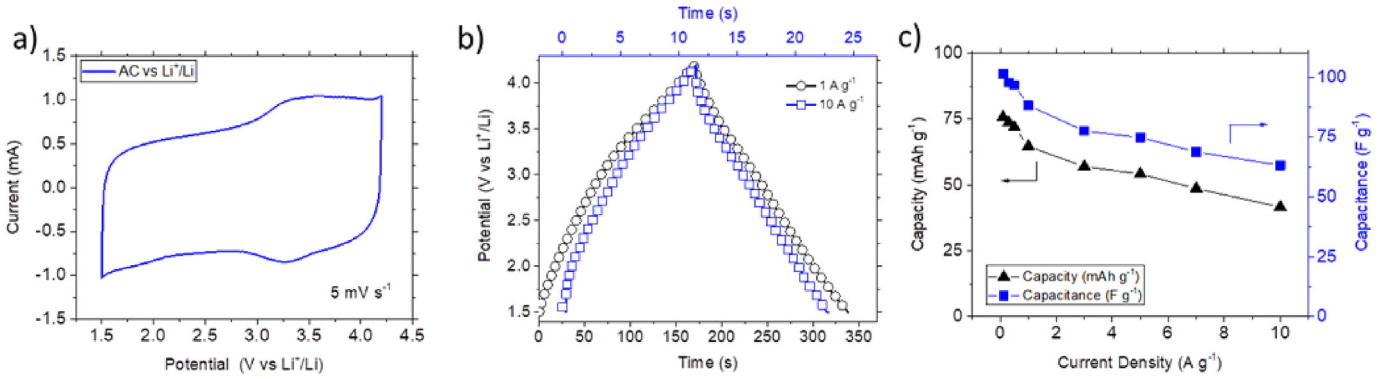

Fig. 6. Electrochemical characterization of the AC tested in between 1.5 and 4.2 V *vs.* Li^+/Li: a) CV, b) GA charge-discharge profiles at 1 A g^{-1} (x –bottom) and 10 A g^{-1} (x-top) and c) rate capability test.

for a potential window of 1.5–4.2 V *vs.* Li^+/Li. The voltammogram in Fig. 6a exhibits a quadratic profile, indicative of a capacitive charge storage mechanism. Interestingly, the capacitance contribution upon positive polarization over the OCP (set at 2.9 V), where PF_6^- ions are electrosorbed into the carbon micropores, is much higher than the contribution upon negative polarization, where Li^+ ions are electrosorbed into the carbon micropores. This is likely related to the bigger solvated size of Li^+ with respect to PF_6^-, inducing some ion-sieving effects below the OCP potential [46–49]. Fig. 6b shows GA charge-discharge profiles of the AC at low and high rates (*i.e.* 1 A g^{-1} and 10 A g^{-1}), with a discharge time of 168 s and 12 s, respectively. As can be seen, the IR drop increment is almost negligible and the profile is ideally symmetric in both cases. As with the HC, a stability test was run within its full operative potential window (1.5–4.2 V *vs.* Li^+/Li) at 10 A g^{-1}, showing a capacity retention of 81% after 10,000 cycles (see Fig. S2). Fig. 6c shows the capacity and capacitance evolution *vs.* the current density. Although in supercapacitor technology charge storage capability is described in terms of capacitance, for the sake of clarity, capacity will be used for comparison with the negative electrode and the overall full hybrid system.

In order to obtain a baseline for the LIC technology comparison (since we have made no attempts to optimize the particle size distribution of the FA-derived activated carbon or the density of the electrode fabricated from this AC), an EDLC based on two symmetric FA-derived ACs was first build (onwards FA-EDLC). In addition, to evaluate the quality of the FA-EDLC, a widely studied and commercially availabe YP50F was used to build a benchmark EDLC

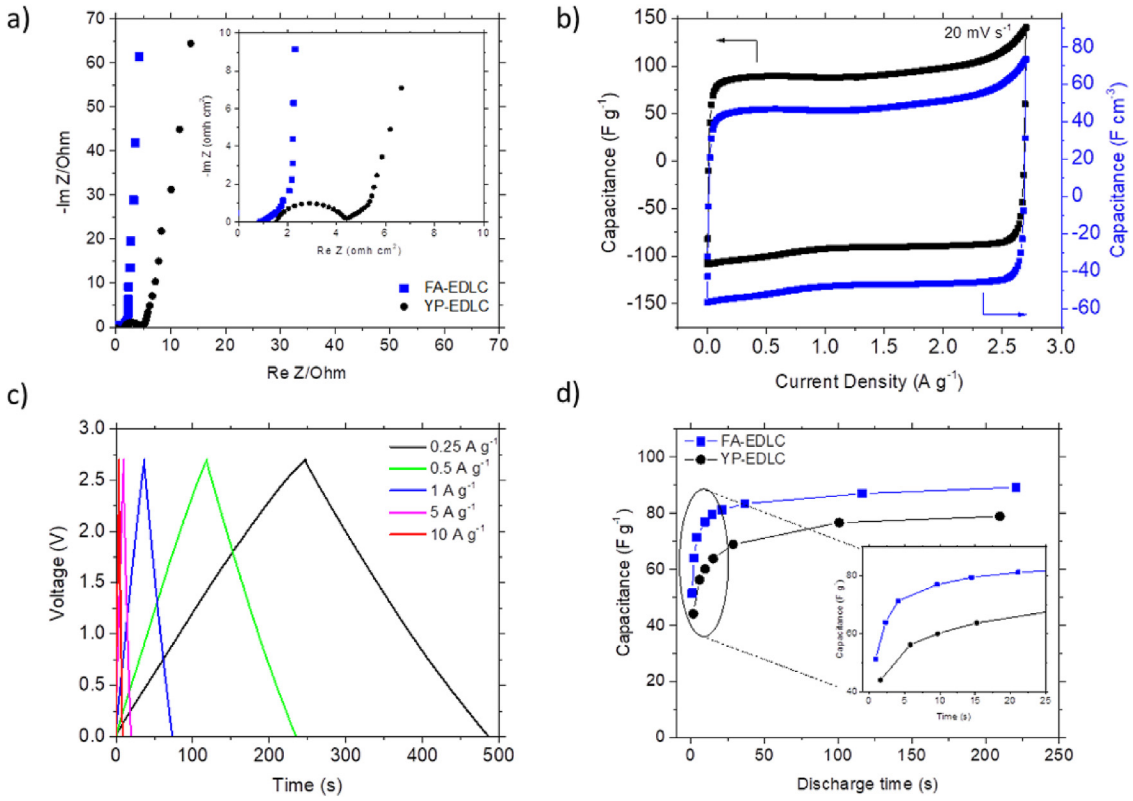

Fig. 7. Electrochemical characterization and comparison of an EDLC fabricated with two symmetric FA derived ACs (FA-EDLC) *vs.* commercially available YP50F based EDLC (YP-EDLC) in 1.5 M Et_4NBF_4 (ACN) tested between 0 and 2.7 V: a) EIS comparative, b) CV, c) GA charge-discharge profiles and d) comparison of capacitance *vs.* discharge time.

(onwards YP-EDLC). Compared to YP-EDLC, Fig. 7a shows a quasi ideal nyquist plot for the FA-EDLC, with very low ohmic resistance and a pure capacitive straight line plot beyond that. Fig. 7b shows CVs - in gravimetric and volumetric terms - at an applied 20 mV s^{-1} scan rate for the FA-EDLC. The voltammogram shows an almost perfect rectangular shape, indicative of a capacitive charge storage mechanism and confirming the low resistance of the system. The calculated mean specific gravimetric capacitance value is *ca.* 100 F g^{-1}. Furthermore, the GA charge-discharge profiles shown in Fig. 7c are perfectly symmetric and exhibit a low voltage drop, in good agreement with the obtained results so far. The specific capacitance values are calculated at different current densities from the GA charge-discharge experiment for both FA- and YP-EDLC systems and are represented *vs.* discharge time in Fig. 7d, both showing good capacitance retention even at very short discharge times. Nevertheless, the capacitance output for the FA-EDLC is slightly higher through all over the discharge times, differences getting more noticeable at high rates, below 1 min discharge time.

Once the EDLC system was evaluated, LICs were assembled using the AC and HC electrodes tested so far. In Fig. 8a, capacities of both HC and AC at different applied current density values are shown. It is clear that the HC outperforms the AC in terms of capacity through all the applied current density range. Since LIC technology is envisaged for high power applications, the aim is to cover the EDLC application range, but offer higher energy. With this in mind, the mass ratio (HC:AC) is adjusted to maximize the performance at high current densities. At the highest applied current density of 10 A g^{-1}, the AC delivers 42 mAh g^{-1} while the HC is capable of 135 mAh g^{-1}, suggesting a 1:3 HC:AC mass ratio. Nevertheless, this will imply the use of the whole potential window of the HC, reaching values close to 0 V *vs.* Li^+/Li, with the inherent risk of lithium plating and consequently faster degradation of the electrode. Thus, for the sake of safety and stability, a 1:2 HC:AC mass ratio was targeted instead. Also, in order to maximize output voltage, maintain safety and compensate for the lithium used to form the SEI in the first cycle, both electrodes were preconditioned. The HC electrode was preconditioned for 5 cycles at a C/10 and then a cut-off potential of 0.2 V *vs.* Li^+/Li was set; while the AC electrode was charged to a cut-off potential of 4.2 V *vs.* Li^+/Li (see Fig. 8b). In Fig. 8c GA charge-discharge profiles of each electrode together with the full hybrid LIC cell operating in the voltage window of 1.5–4.2 V are shown, at an applied current density of 1 A g^{-1}, indicating a discharge time of 154 s. At this rate, the system behaves as an ideal capacitor, with a highly symmetric charge-discharge profile, confirming that the capacitive mechanism governs the overall charge storage mechanism, despite the introduction of the faradaic HC electrode. It turns out that despite the challenging discharge times here (154 s), new generations of ultrafast batteries can already perform at this level [50]. So we investigate a 10-fold increase in the current density – decreasing the discharge time to 9 s (shown in Fig. 8d). This rate is clearly in the EDLC application range, and at this point there is no battery fast enough to accommodate these high charge-discharge rates. Despite the fact that the LIC shows a slight rise in the IR drop in Fig. 8d, together with some polarization at the charging step -owing to the polarization of the HC electrode- the capacitive storage mechanism still dominates the device behavior at this high charge-discharge rate.

In order to evaluate how this performance translates into energy-to-power ratios, a Ragone plot comparing the FA-derived carbon-based LIC with its EDLC counterpart, is shown in Fig. 9a. Reported values here refer to the sum of the active mass (AM) of both electrodes (mg of HC + mg of AC). For an application where the desired discharge time is *ca.* 1 min, the EDLC can offer 20 Wh kg^{-1}_{AM} at 1.1 kW kg^{-1}_{AM}. Meanwhile, the LIC can offer 110 Wh

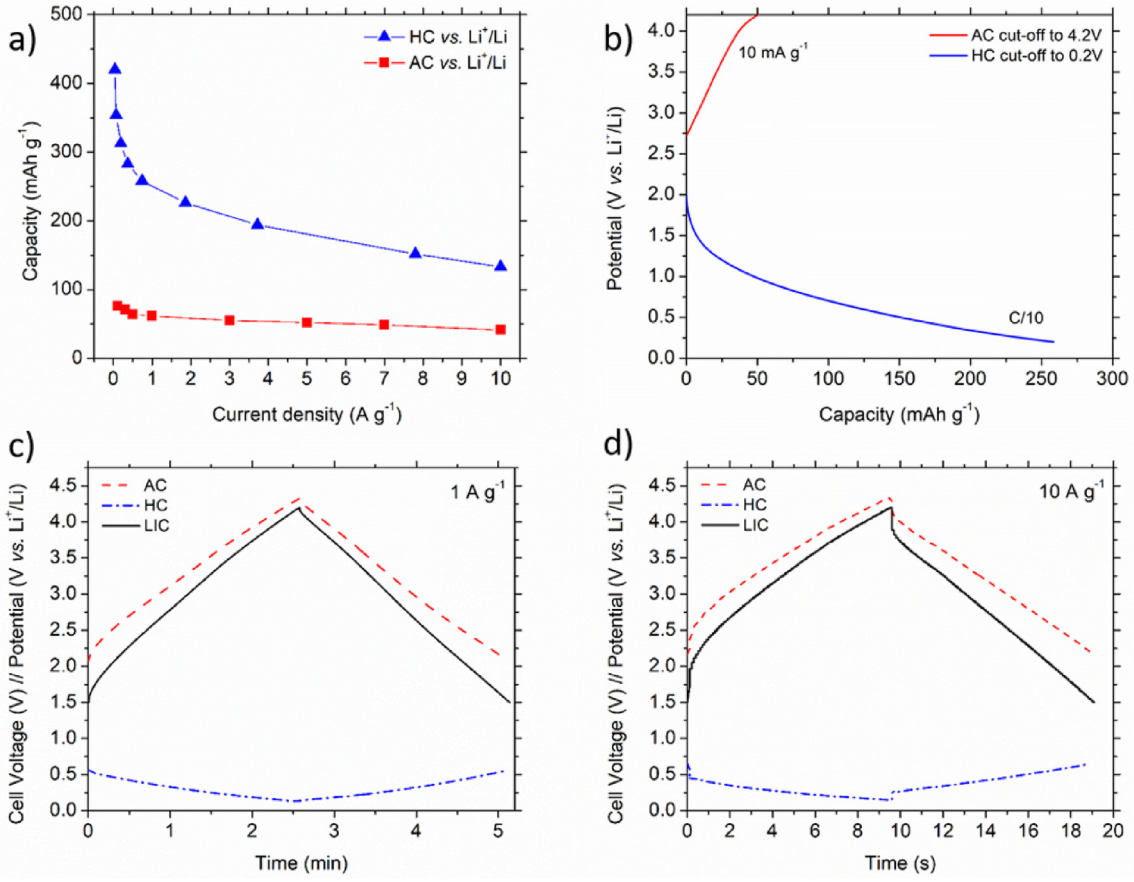

Fig. 8. a) Capacity of HC *vs.* AC at different applied current densities, b) electrode preconditioning step, c) and d) GA charge-discharge profiles for the LIC system characterized between 1.5 and 4.2 V and each of the electrodes at an applied current density of 1 A g^{-1} and 10 A g^{-1}, respectively.

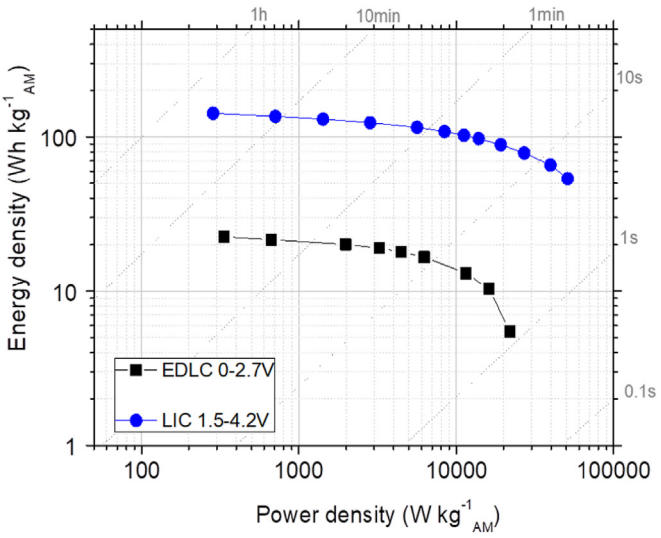

Fig. 9. a) Ragone Plot respect to total active mass comparing FA derived carbon based EDLC and LIC technologies.

kg^{-1}_{AM} at 7 kW kg^{-1}_{AM}, showing a 5-fold increase of energy with an almost 6 kW kg^{-1}_{AM} gain in power. This means that the LIC has not only more energy but also more power than the equivalent EDLC. When the discharge time is reduced to only 10 s, the EDLC delivers 16 Wh kg^{-1}_{AM} at 7 kW kg^{-1}_{AM} while the LIC delivers 70 Wh kg^{-1}_{AM} at 25 kW kg^{-1}_{AM} offering a 4-fold increase in energy and power. In addition, the cyclability test run at 10 A g^{-1} showed capacitance retention of 83% after 10,000 cycles (see Fig. S3).

4. Conclusions

We have described the synthesis of a HC and an AC using different processing conditions of the same furfuryl alcohol precursor material. The HC's specific structural and textural properties (*e.g.* SSA values of >200 m^2 g^{-1}) show attractive performance in high power applications. In addition, milling the HC particles to sub-micron sizes, along with an electrode fabrication method that keeps the material loading to <1.5 mg cm^{-2}, enabled the development of an ultrafast negative electrode with high capacities at high rates (~100 mAh g^{-1} at 50C). This HC-based negative electrode, along with an AC electrode also based on the furfuryl alcohol precursor, was used to fabricate a LIC with a carbon loading of 1:2 (HC:AC mass ratio). The LIC showed excellent high-energy properties, exceeding the highly challenging energy density barrier of 100 Wh kg^{-1}_{AM} at a high power of 10 kW kg^{-1}_{AM}, with a sub-minute discharge time. The fastest discharge time reached was around 10 s, and the LIC delivered 50 Wh kg^{-1}_{AM} at 50 kW kg^{-1}_{AM} under those conditions. The LIC also achieved good cycle life, retaining 83% of the initial capacitance after 10,000 cycles at 10 A g^{-1}. Not only are furfuryl alcohol-based carbons a viable option for energy storage applications, they are also derived from a biomass-based renewable resource and represent a platform

technology with flexibility in terms of textural and structural properties that allow the synthesis of carbons ranging from a low SSA HC to a high SSA AC.

Acknowledgments

The authors would like to thank financial support by the Basque Country Government under the Elkartek 18 program (Projects CICE2018) and by the Spanish Ministry of Economy and Competitiveness (MINECO/FEDER) through the project MATCAP (MAT2015-64617-C2-2-R). M. Arnaiz thanks the Spanish Ministry of Science, Innovation and Universities for her FPU pre-doctoral fellowship (FPU15/04876).

Appendix A. Supplementary data

Supplementary data to this article can be found online at https://doi.org/10.1016/j.electacta.2019.03.029.

References

[1] M.R. Lukatskaya, B. Dunn, Y. Gogotsi, Multidimensional materials and device architectures for future hybrid energy storage, Nat. Commun. 7 (2016) 12647. https://doi.org/10.1038/ncomms12647.
[2] J. Ding, W. Hu, E. Paek, D. Mitlin, Review of hybrid ion capacitors: from aqueous to lithium to sodium, Chem. Rev. 118 (2018) 6457. https://doi.org/10.1021/acs.chemrev.8b00116.
[3] S.-D. Xu, Y. Zhao, S. Liu, X. Ren, L. Chen, W. Shi, X. Wang, D. Zhang, Curly hard carbon derived from pistachio shells as high-performance anode materials for sodium-ion batteries, J. Mater. Sci. 53 (2018) 12334. https://doi.org/10.1007/s10853-018-2472-4.
[4] JM Energy Company website https://www.jmenergy.co.jp/en/
[5] H. Wang, M. Yoshio, Performance of AC/graphite capacitors at high weight ratios of AC/graphite, J. Power Sources 177 (2008) 681. https://doi.org/10.1016/j.jpowsour.2007.11.066.
[6] W. Cao, J. Zheng, D. Adams, T. Doung, J.P. Zheng, Comparative study of the power and cycling performance for advanced lithium-ion capacitors with various carbon anodes, J. Electrochem. Soc. 161 (2014) A2087. https://doi.org/10.1149/2.0431414jes.
[7] T. Aida, K. Yamada, M. Morita, An advanced hybrid electrochemical capacitor that uses a wide potential range at the positive electrode, Electrochem. Solid State Lett. 9 (2006) A534. https://doi.org/10.1149/1.2349495.
[8] S.R. Sivakkumar, A.G. Pandolfo, Evaluation of lithium-ion capacitors assembled with pre-lithiated graphite anode and activated carbon cathode, Electrochim. Acta 65 (2012) 280. https://doi.org/10.1016/j.electacta.2012.01.076.
[9] W. Lv, F. Wen, J. Xiang, J. Zhao, L. Li, L. Wang, Z. Liu, Y. Tian, Peanut shell derived hard carbon as ultralong cycling anodes for lithium and sodium batteries, Electrochim. Acta 176 (2015) 533. https://doi.org/10.1016/j.electacta.2015.07.059.
[10] Y. Sun, J. Tang, F. Qin, J. Yuan, K. Zhang, J. Li, D.-M. Zhu, L.-C. Qin, Hybrid lithium-ion capacitors with asymmetric graphene electrodes, J. Mater. Chem. 5 (2017) 13601. https://doi.org/10.1039/C7TA01113J.
[11] J. Ajuria, M. Arnaiz, C. Botas, D. Carriazo, R. Mysyk, T. Rojo, A.V. Talyzin, E. Goikolea, Graphene-based lithium ion capacitor with high gravimetric energy and power densities, J. Power Sources 363 (2017) 422. https://doi.org/10.1016/j.jpowsour.2017.07.096.
[12] K. Naoi, S. Ishimoto, Y. Isobe, S. Aoyagi, High-rate nano-crystalline $Li_4Ti_5O_{12}$ attached on carbon nano-fibers for hybrid supercapacitors, J. Power Sources 195 (2010) 6250. https://doi.org/10.1016/j.jpowsour.2009.12.104.
[13] E. Zhao, C. Qin, H.-R. Jung, G. Berdichevsky, A. Nese, S. Marder, G. Yushin, Lithium titanate confined in carbon nanopores for asymmetric supercapacitors, ACS Nano 10 (2016) 3977. https://doi.org/10.1021/acsnano.6b00479.
[14] N. Xu, X. Sun, X. Zhang, K. Wang, Y. Ma, A two-step method for preparing $Li_4Ti_5O_{12}$ graphene as an anode material for lithium-ion hybrid capacitors, RSC Adv. 5 (2015) 94361. https://doi.org/10.1039/C5RA20168C.
[15] E. Iwama, N. Kawabata, N. Nishio, K. Kisu, J. Miyamoto, W. Naoi, P. Rozier, P. Simon, K. Naoi, Enhanced electrochemical performance of ultracentrifugation-derived nc-Li_3VO_4/MWCNT composites for hybrid supercapacitors, ACS Nano 10 (2016) 5398. https://doi.org/10.1021/acsnano.6b01617.
[16] H.-Y. Wei, D.-S. Tsai, C.-L. Hsieh, A prelithiated lithium vanadate anode and the mass balancing of its hybrid capacitor, RSC Adv. 5 (2015) 69176. https://doi.org/10.1039/C5RA11664C.
[17] M. Arnaiz, J.L. Gómez-Cámer, F. Mijangos, T. Rojo, E. Goikolea, J. Ajuria, Novel lithium-ion capacitor based on TiSb2 as negative electrode: the role of mass ratio towards high energy-to-power densities and long cyclability, Batteries & Supercaps, in the press. https://doi.org/10.1002/batt.201800114
[18] M. Arnaiz, C. Botas, D. Carriazo, R. Mysyk, F. Mijangos, T. Rojo, J. Ajuria, E. Goikolea, Reduced graphene oxide decorated with SnO2 nanoparticles as negative electrode for lithium ion capacitors, Electrochim. Acta, 284 542-550. https://doi.org/10.1016/j.electacta.2018.07.189
[19] S. Zhang, C. Li, X. Zhang, X. Sun, K. Wang, Y. Ma, High performance lithium-ion hybrid capacitors employing Fe_3O_4/Graphene composite anode and activated carbon cathode, ACS Appl. Mater. Interfaces 9 (2017) 17136. https://doi.org/10.1021/acsami.7b03452.
[20] C. Han, H. Li, R. Shi, L. Xu, J. Li, F. Kang, B. Li, Nanostructured anode materials for non-aqueous lithium ion hybrid capacitors, Energy & Environmental Materials 1 (2018) 75. https://doi.org/10.1002/eem2.12009.
[21] M. Schroeder, M. Winter, S. Passerini, A. Balducci, On the cycling stability of lithium-ion capacitors containing soft carbon as anodic material, J. Power Sources 238 (2013) 388. https://doi.org/10.1016/j.jpowsour.2013.04.045.
[22] M. Schroeder, M. Winter, S. Passerini, A. Balducci, On the use of soft carbon and propylene carbonate-based electrolytes in lithium-ion capacitors, J. Electrochem. Soc. 159 (2012) A1240. https://doi.org/10.1149/2.050208jes.
[23] W.J. Cao, J.P. Zheng, Li-ion capacitors with carbon cathode and hard carbon/stabilized lithium metal powder anode electrodes, J. Power Sources 213 (2012) 180–185. https://doi.org/10.1016/j.jpowsour.2012.04.033.
[24] X. Sun, X. Zhang, H. Zhang, N. Xu, K. Wang, Y. Ma, High performance lithium-ion hybrid capacitors with pre-lithiated hard carbon anodes and bifunctional cathode electrodes, J. Power Sources 270 (2014) 318. https://doi.org/10.1016/j.jpowsour.2014.07.146.
[25] P. Jezowski, O. Crosnier, E. Deunf, P. Poizot, F. Beguin, T. Brousse, Safe and recyclable lithium-ion capacitors using sacrificial organic lithium salt, Nat. Mater. 17 (2018) 167. https://doi.org/10.1038/nmat5029.
[26] W.J. Cao, J.P. Zheng, Li-ion Capacitors with Carbon Cathode and Hard Carbon/stabilized Lithium Metal Powder Anode Electrodes, vol. 213, 2012, p. 180. https://doi.org/10.1016/j.jpowsour.2012.04.033.
[27] J. Yan, W.J. Cao, J.P. Zheng, Constructing high energy and power densities Li-ion capacitors using Li thin film for pre-lithiation, J. Electrochem. Soc. 164 (2017) A2164. https://doi.org/10.1149/2.1701709jes.
[28] J. Ronsmans, Roll-to-roll prelithiation for lithium ion battery anodes, in: AABC Europe, Strasbourg, France, 28-29 January 2019.
[29] Z. Gao, Y. Zhang, N. Song, X. Li, Biomass-derived renewable carbon materials for electrochemical energy storage, Materials Research Letters 5 (2017) 69. https://doi.org/10.1080/21663831.2016.1250834.
[30] L. Wu, D. Buchholz, C. Vaalma, G.A. Giffin, S. Passerini, Apple-biowaste-derived hard carbon as a powerful anode material for Na-ion batteries, ChemElecroChem 3 (2015) 292. https://doi.org/10.1002/celc.201500437.
[31] E.M. Lotfabad, J. Ding, K. Cui, A. Kohandehghan, W.P. Kalisvaart, M. Hazelton, D. Mitlin, High-density sodium and lithium ion battery anodes from banana peels, ACS Nano 8 (2014) 7115. https://doi.org/10.1021/nn502045y.
[32] J. Ajuria, E. Redondo, M. Arnaiz, R. Mysyk, T. Rojo, E. Goikolea, Lithium and sodium ion capacitors with high energy and power densities based on carbons from recycled olive pits, J. Power Sources, 359 17-26. https://doi.org/10.1016/j.jpowsour.2017.04.107
[33] K. Sun, S. Yu, Z. Hu, Z. Li, G. Lei, Q. Xiao, Y. Ding, Oxygen-containing hierarchically porous carbon materials derived from wild jujube pit for high-performance supercapacitor, Electrochim. Acta 231 (2017) 417. https://doi.org/10.1016/j.electacta.2017.02.078.
[34] A. Raj K, M.R. Panda, D.P. Dutta, S. Mitra, Bio-derived mesoporous disordered carbon: an excellent anode in sodium-ion battery and full-cell lab prototype, Carbon 143 (2019) 402. https://doi.org/10.1016/j.carbon.2018.11.038.
[35] L. Cao, W. Hui, Z. Xu, J. Huang, P. Zheng, J. Li, Q. Sun, Rape seed shuck derived-lamellar hard carbon as anodes for sodium-ion batteries, J. Alloy. Comp. 695 (2017) 632. https://doi.org/10.1016/j.jallcom.2016.11.135.
[36] W. Li, M. Chen, C. Wang, Spherical hard carbon prepared from potato starch using as anode material for Li-ion batteries, Mater. Lett. 65 (2011) 3368–3370. https://doi.org/10.1016/j.matlet.2011.07.072.
[37] X. Liu, H. Wang, Y. Cui, X. Xu, H. Zhang, G. Lu, J. Shi, W. Liu, S. Chen, X. Wang, High-energy sodium-ion capacitor assembled by hierarchical porous carbon electrodes derived from Enteromorpha, J. Mater. Sci. 53 (2018) 6763. https://doi.org/10.1007/s10853-017-1982-9.
[38] A. Beda, P.-L. Taberna, P. Simon, C.l. Matei Ghimbeu, Hard carbons derived from green phenolic resins for Na-ion batteries, Carbon 139 (2018) 248–257. https://doi.org/10.1016/j.carbon.2018.06.036.
[39] J. Ni, Y. Huang, L. Gao, A high-performance hard carbon for Li-ion batteries and supercapacitors application, J. Power Sources 223 (2013) 306–311. https://doi.org/10.1016/j.jpowsour.2012.09.047.
[40] Z. Yuan, L. Si, X. Zhu, Three-dimensional hard carbon matrix for sodium-ion battery anode with superior-rate performance and ultralong cycle life, J. Mater. Chem. 3 (2015) 23403. https://doi.org/10.1039/C5TA07223A.
[41] Y. Nishi, H. Azuma, A. Omaru, Non Aqueous Electrolyte Cell, US Patent #4959281, (1990).
[42] H. Imoto, A. Omaru, H. Azuma, Y. Nishi, Y. Gonno, M. Nagamine, US Patent #5643426, (1997).
[43] S. Mitra, V. Nair, Method of Making Hard Carbon Materials, US Patent Publication #2018/0375093A1, (2018).
[44] S. Mitra, A Method of Making Activated Nano-Porous Carbon, US patent #9938152 (2018).
[45] R. Väli, A. Jänes, E. Lust, Alkali-metal insertion processes on nanospheric hard carbon electrodes: an electrochemical impedance spectroscopy study, J. Electrochem. Soc. 164 (2017) E3429. https://doi.org/10.1149/2.0431711jes.

[46] L. Eliad, G. Salitra, A. Soffer, D. Aurbach, Ion sieving effects in the electrical double layer of porous carbon electrodes: estimating effective ion size in electrolytic solutions, J. Phys. Chem. B 105 (2001) 6880. https://doi.org/10.1021/jp010086y.

[47] Y. Kameda, Y. Umebayashi, M. Takeuchi, M.A. Wahab, S. Fukuda, S.-i. Ishiguro, M. Sasaki, Y. Amo, T. Usuki, Solvation structure of Li^+ in concentrated $LiPF_6$ propylene carbonate solutions, J. Phys. Chem. B 111 (2007) 6104. https://doi.org/10.1021/jp072597b.

[48] X. Sun, X. Zhang, W. Liu, K. Wang, C. Li, Z. Lia, Y. Ma, Electrochemical performances and capacity fading behaviors of activated carbon/hard carbon lithium ion capacitor, Electrochim. Acta 235 (2017) 158. https://doi.org/10.1016/j.electacta.2017.03.110.

[49] F. Sun, J. Gao, X. Liu, L. Wang, Y. Yang, X. Pi, S. Wu, Y. Qin, High-energy Li-Ion Hybrid Supercapacitor Enabled by a Long Life N-Rich Carbon Based Anode, vol. 213, 2016, p. 626. https://doi.org/10.1016/j.electacta.2016.08.004.

[50] Z. Yao, X. Xia, D. Xie, Y. Wang, C.-a. Zhou, S. Liu, S. Deng, X. Wang, J. Tu, Enhancing ultrafast lithium ion storage of $Li_4Ti_5O_{12}$ by tailored TiC/C core/shell skeleton plus nitrogen doping, Adv. Funct. Mater. 28 (2018) 1802756. https://doi.org/10.1002/adfm.201802756.